International Journal of Pharmaceutical Science and Research
www.pharmacyjournal.net
ISSN: 2455-4685
Received: 13-04-2026, Accepted: 14-05-2026, Published: 29-05-2026
Volume 11, Issue 2, 2026, Page No. 32-48

Mechanistic evaluation of *Acalypha indica* HIC Fraction: Induction of ROS-Dependent DNA Damage and ATR–Chk1 Mediated Apoptosis in Cervical Cancer

Thangadurai K[1*], Abhirami M[2], Nithya S[3], Manickam V[2], Kumarakurubarn DA[4], Latha M[5]
[1] Principal, JSA Medical College for Siddha and Research Centre, Tamil Nadu, India
[2] Siddha Physician, Sri Ramana Herbal Centre, Tamil Nadu, India
[3] Department of Botany, Arignar Anna Government Arts College, Namakkal, Tamil Nadu, India
[4] Associate Professor, National Institute of Siddha, Chennai, Tamil Nadu, India
[5] Medical Superintendent, Shri Indra Ganesan Siddha Medical College and Hospital, Trichy, Tamil Nadu, India

Abstract
Acalypha indica is a medicinal plant widely used in traditional healthcare systems and is known for its diverse pharmacological properties. The present study aimed to evaluate the anticancer potential of its hexane-insoluble chloroform (HIC) fraction against cervical cancer cell lines, including HeLa (HPV-18 positive), SiHa (HPV-16 positive), and C33A (HPV-negative). Phytochemical characterization using GC–MS and LC–MS revealed the presence of various bioactive compounds such as alkaloids, phenolic, terpenoids, and fatty acids, including squalling, ruin, catching, and linoleic acid.
Biological assays demonstrated that the HIC fraction significantly induced cytotoxicity and apoptosis in all tested cell lines, as confirmed by Annexing V-FITC/PI staining and morphological changes. Cell cycle analysis revealed sub-G0 accumulation in HeLa and C33A cells, while G1/S phase arrest was observed in SiHa cells. Gene and protein expression studies indicated up regulation of pro-apoptotic markers (p53, Bax, p21, and cleaved caspase-3) and down regulation of anti-apoptotic and oncogenic markers (Bcl-2 and HPV E6).
Furthermore, the treatment induced reactive oxygen species (ROS) generation, mitochondrial membrane potential loss, and significant DNA damage, as evidenced by γH2AX incorporation and activation of AT Signalling pathways.
These findings suggest that ROS-mediated DNA damage plays a crucial role in triggering apoptosis. Overall, the study concludes that the HIC fraction of *Acalypha indica* exhibits potent anticancer activity against cervical cancer cells and holds promise as a potential source for the development of novel therapeutic agents.

Keywords: *Acalypha indica*, cervical cancer, Apoptosis, ROS generation, DNA damage, ATR–Chk1 pathway, GC–MS, LC–MS, Siddha Medicine.

Introduction

Acalypha indica is a widely distributed annual herb commonly found in household backyards and informal settlements across the plains of India. This plant has long been valued in traditional medicine for treating respiratory conditions such as bronchitis, pneumonia, asthma, and pulmonary tuberculosis, as it acts as an emetic, expectorant, purgative, and diuretic. (Ahmadi M, *et al*., 2024) [1] In homeopathic practice, it is used to manage severe respiratory symptoms, including persistent coughing, lung-related complications, haemoptysis, and early-stage tuberculosis. Additionally, the plant is known for its significant antioxidant and anticancer properties. (AlMousa LA, Pandey P*, et al.,* 2025) [2]. In recent years, there has been growing interest in studying plant-derived secondary metabolites as potential therapeutic agents. Many bioactive compounds obtained from plants are currently being explored for their effectiveness in modern pharmacology. (Balachandran A, *et al.,2023* [4]) Traditional medicinal systems, especially those based on medicinal plants, remain essential for meeting primary healthcare needs in many developing countries. (Bray F, *et* al., 2024) [5].
Acalypha indica, commonly known as Indian copperleaf or Indian mercury, is a medicinal plant belonging to the Euphorbiaceae family and has been reported to exhibit post-coital antifertility effects. (Bykov VJ, *et al.,* 2022) [6] In traditional medicine, the entire plant as well as its leaves are widely used for treating skin wounds and as an antidote for venomous bites. (Chapkin RS, *et al., 2022)* [8]. Scientific investigations have confirmed that the leaves possess antibacterial, anti-inflammatory, and antioxidant properties (Chekuri S, *et al*., 2023) [9]. Several studies have also focused on isolating and identifying phytochemical constituents from its leaf extracts, with some analyses carried out using GC–MS techniques. In the present study, methanol extracts of *Acalypha indica* were subjected to GC–MS analysis, along with evaluation using the Prediction of Activity Spectra for Substances (PASS) approach. (Dilkalal A, *et al*., 2024) [11].
The research specifically aimed to examine the interaction of a key phytochemical, 2-methoxy-4-vinylphenol, with important target proteins such as JAK2 kinase, retinoblastoma protein (pRB), and COX-2. (Du, C., *et al*. 2026). This investigation was conducted to generate new insights that could contribute to the development of effective anticancer and anti-inflammatory therapeutic agents. (Hayati EK, Sabarudin A., 2025) [14].
In this study, we aimed to assess the potential of this traditional medicinal plant against cervical cancer cell lines. Cancer cells are marked by abnormal regulation of the cell

cycle, leading to excessive cell proliferation and resistance to programmed cell death (apoptosis), which contributes to their continuous survival. (Hayati EK, *et* al., 2025) [14]. Targeting these cells through induced cell death is therefore an important therapeutic strategy. For this investigation, three cervical cancer cell lines were selected: HeLa (HPV-18 positive), SiHa (HPV-16 positive), and C33A (HPV-negative), allowing a comparison of the plant extract's effects on both HPV-positive and HPV-negative cells. (Huang, S., *et a*l., 2025) [16]. Additionally, the study focused on identifying the specific mechanisms of cell death triggered by the plant extract in these cell lines.

Materials and Methods

Collection and Authentication of Plant Material

Leaves of *Acalypha indica* is collected from Karkudalpatti village, Rasipuram Taluk, Tamil Nadu, during the post-monsoon season. Plant selection was based on local ethno medicinal knowledge. The materials were washed, taxonomically authenticated using standard floras, and a voucher specimen number is 975 at BSI (Botanical Survey of India, Coimbatore) was deposited in the departmental herbarium.

Processing of Plant and Extraction

The whole plant material was first washed thoroughly with tap water and then rinsed with distilled water to minimize contamination acquired during handling and transportation. (Islam, M. A., *et al*., 2024) [17]. It was subsequently shade-dried for a period of one month. For extraction, various solvents including petroleum ether, chloroform, methanol, ethanol, isopropanol, ethyl acetate, and distilled water were employed. Approximately 20 g of powdered leaves and stems were soaked in 150 mL of each solvent in separate conical flasks and stirred thoroughly using a glass rod to facilitate efficient extraction. (Islam, S. I., *et al.,* 2025) [18]. The mixtures were left undisturbed at room temperature for 24 hours. After incubation, the extracts were filtered through what man No. 1 filter paper (125 mm × 100 circles) and collected for further analysis. Phytochemical screening was carried out using standard qualitative methods, while quantitative estimations were performed for key constituents such as phenols, flavonoids, alkaloids, and glycosides. (Kalsoom A, *et al.,* 2025).

GC–MS Analysis

The samples were derivatives using BSTFA (Sigma) to form TMS derivatives prior to analysis. They were then injected into an HP5-MS capillary column (30 m × 0.25 mm × 0.25 µm) and subjected to a temperature program ranging from 70°C to 260°C, with a heating rate of 5°C per minute (Agilent system). The resulting mass spectra were analysed, and the fragmentation patterns of the detected compounds were compared with those available in the NIST library for identification. (Kiran A, *et al.,* 2023) [20].

LC–MS/MS Analysis

The chloroform fraction of the sample was first dried under a gentle nitrogen stream and then reconstituted in methanol for analysis. The chemical constituents were examined using LC–MS/MS, where a UPLC system was coupled with a hybrid quadruple orthogonal time-of-flight (Q-TOF) tandem mass spectrometer (SYNAPT G2 HDMS, Waters, Manchester, UK) equipped with an electrospray ionization (ESI) source. Chromatographic separation was achieved using an Acquit UPLC BEH C18 column (3.0 mm × 150 mm, 1.7 µm, Waters, Ireland) maintained at 40°C. (Nair PMK, Pandian AR, *et al*., 2025) [23] The mobile phase consisted of solvent A (0.1% formic acid in water) and solvent B (0.1% formic acid in acetonitrile), delivered at a flow rate of 0.4 mL/min. A linear gradient elution program was applied: 20–80% B from 0 to 15 minutes, 80–95% B from 15.0 to 15.5 minutes, maintained at 95% B until 18.0 minutes, then reduced to 20% B from 18.0 to 19.0 minutes, and finally held at 25% B from 19.0 to 20.0 minutes. (Qian S, Wei Z, Yang W, *et al.,* 2024).

The mass spectrometer operated under the following conditions: capillary voltage of 3 kV (ESI+ mode), sample cone voltage of 35 V, extraction cone voltage of 4 V, source temperature of 100°C, and desolation temperature of 300°C. (Rekha M*, et al.,* 2024) [26]. The cone gas flow was set at 50 L/h, and desolation gas flow at 800 L/h. Data were acquired in MSE mode, with a trap collision energy of 5 eV for low-energy scans and a ramped collision energy of 20–50 eV for high-energy scans. Argon was used as the collision gas for collision-induced dissociation (CID). To maintain mass accuracy and reproducibility, the instrument was calibrated over a mass range of 50–1500 Da using sodium format solution. (Sharma D, Singh C, *et al.,* 2025) [31]. The obtained spectra were analysed by comparing them with data from established compound databases for identification. (Shimu MSS, Paul GK, *et al.,* 2025) [33].

Table 1: Primer sequences and PCR profiles of the genes analysed in RT-PCR

Gene	Primer sequence (5'→ 3')	
	Forward	Reverse
p53	ATGGCCATCTACAAGCAG	ACAGTCAAGAGCCAACCTCAG
p21	ATGAAATTCACCCCCTTTCC	CCCTAGGCTGTGCTCACTTC
BAX	GTGGCAGCTGACATGTTTTC	GGAGGAAGTCCAATGTCCAG
Bcl-2	GGGTACGATAACCGGGAGAT	CTGAAGAGCTCCTCCACCAC
ET-1	TCCTCTGCTGGTTCCTGACT	CAGAAACTCCACCCCTGTGT
HPV 16 E6	TTGCTTTTCGGGATTTATGC	CAGGACACAGTGGCTTTTGA
HPV 18 E6	TGAAAAACGACGATTCCACA	TTGTGTTTCGCGTCGTT
GAPDH	CAAGGTCATCCATGACAACTTTG	GTCCACCACCCTGTTGCTGTAG

PCR profile

	Initial denaturation C - minutes)	Denaturation (°C - seconds)	Annealing (°C – seco (°nds	Extension (°C – seconds	Number of cycles	Final extension (°C - minutes)	Product length (bp)
p53			58 – 30	72 – 45			210
p21			58 – 30	72 – 30			174
BAX			58 – 30	72 – 45			151

Bcl-2			58 – 30	72 – 45			395
	94-4	94-30			35	72 – 7	
ET-1			57 – 30	72 – 45			242
HPV 16 E6			52 – 30	72 – 30			106
HPV 18 E6			53 – 30	72 – 30			285
GAPDH			58 – 30	72 – 45			496

Table 2: Specifications of antibodies, along with their respective dilutions.

Protein	Manufacturer	Code	Reactivity	Dilution	Experiment
Caspase-3	Cell Signaling Technology	9665	Rabbit monoclonal	1:1000	
BAX		Sc-7480			
Bcl-2		Sc-509			
	Santa Cruz Biotechnology				
p53		Sc-126	Mouse monoclonal	1:500	
p21		Sc-6246			
HPV 16/18 E6	AbCam	Ab-70			
ß-tubulin	Sigma	T8328	Mouse monoclonal	1:5000	Western Blot
p-ATR		2853			
p-ATM		5883			
	Cell Signaling Technology	2349	Rabbit polyclonal (p-ATM monoclonal)	1:1000	
p-Chk1		2661			
p-Chk2		Sc-2007			
Goat anti-Rabbit IgG – AP	Santa Cruz Biotechnology	ADI-SAB-101	Rabbit	1:5000	
Goat anti-Mouse IgG – AP	Enzo Life Science	9718	Mouse		
γ-H2AX	Cell Signaling Technology	F0382	Rabbit monoclonal	1:50	Indirect Immuno Fluorescence
Goat anti-Rabbit oIgG-FITC	Sigma		Rabbit		

Column Chromatography and GC–MS Analysis

The chloroform fraction of the extract was concentrated using a rotary evaporator and then blended with silica gel (60–120 mesh) to form a slurry. This mixture was loaded onto a glass column packed with silica gel (60–120 mesh) and sequentially eluted using solvents of increasing polarity, namely hexane, ethyl acetate, and methanol. Fractions were collected at intervals corresponding to half the column bed volume, concentrated, and analysed using thin-layer chromatography (TLC). Similar fractions were combined when appropriate. The pooled fractions were then evaluated for cytotoxic activity using the MTT assay, employing a single concentration equivalent to the IC_{50} value of HIC across different cell lines. (Upadhyay, S., *et al*. 2024) [36]. The assessment focused on determining whether at least 50% cell death occurred (data not shown). Fractions exhibiting significant cytotoxicity were selected for further characterization by GC–MS analysis, following the procedure described previously.

Antioxidant Assay

DPPH Radical Scavenging Method

The antioxidant activity of the plant extract was evaluated using the DPPH radical scavenging assay. A 0.1 mm solution of DPPH was prepared in methanol. To this, 1.0 ml of DPPH solution was mixed with 1.0 mL of plant extract at varying concentrations ranging from 50 to 300 µg/ml. The reaction mixture was then incubated in the dark at room temperature for 30 minutes to allow the reaction to occur. Following incubation, the absorbance was recorded at 517 nm using methanol as a blank. Ascorbic acid was used as the reference standard for comparison. The percentage of free radical inhibition was calculated using the formula.

$$\% \text{ Inhibition} = [(Ac - As) / Ac] \times 100$$

Where *Ac* represents the absorbance of the control and *as* denotes the absorbance of the sample.

ABTS Radical Cat ion Decolourization Assay

The antioxidant potential of the extract was also assessed using the ABTS radical cat ion decolourization method. The ABTS radical was produced by combining a 7 mm ABTS solution with 2.45 mm potassium persulfate, and the mixture was kept in the dark at room temperature for 12–16 hours to allow radical formation. Prior to the assay, this solution was diluted with ethanol to obtain an absorbance of 0.70 ± 0.02 at 734 nm. For the analysis, 1.0 ml of the prepared ABTS solution was mixed with 100 µl of the plant extract at various concentrations. The reaction mixture was incubated for 6 minutes, after which the absorbance was measured at 734 nm. Ascorbic acid was used as the standard reference compound for comparison.

Hydrogen Peroxide (H_2O_2) Scavenging Assay

The hydrogen peroxide scavenging activity of the plant extract was evaluated using a standard method. A 40 mm H_2O_2 solution was prepared in phosphate buffer (50 mm, pH 7.4). To this, 1 mL of the plant extract at different concentrations was added to 0.6 mL of the H_2O_2 solution. The reaction mixture was incubated at room temperature for 10 minutes. After incubation, the absorbance was measured at 230 nm using a blank containing phosphate buffer without hydrogen peroxide. Ascorbic acid was used as the reference standard to compare the scavenging activity.

Superoxide Anion Scavenging Assay

The ability of the plant extract to scavenge superoxide radicals was assessed using a standard assay system. The reaction mixture consisted of 1 mL of nitro blue tetrazolium (NBT, 156 µM), 1 mL of NADH (468 µM), and 1 ml of the plant extract at varying concentrations. The reaction was

initiated by adding 100 µL of phenazine methosulfate (PMS, 60 µM). After incubation at 25°C for 5 minutes, the absorbance was recorded at 560 nm using an appropriate blank. A decrease in absorbance corresponded to an increase in superoxide radical scavenging activity of the extract.

Nitric Oxide (NO) Radical Scavenging Assay

The nitric oxide scavenging activity of the plant extract was evaluated using sodium nitroprusside as a source of nitric oxide. A mixture containing 0.5 mL of sodium nitroprusside (10 mm) in phosphate buffer (pH 7.4) was combined with 0.5 mL of the plant extract at various concentrations and incubated at 25°C for 150 minutes. Following incubation, 0.5 mL of the reaction mixture was treated with 0.5 mL of Gris's reagent, which consists of 1% sulphanilamide, 0.1% naphthyl ethylenediamine dihydrochloride, and 2% phosphoric acid. The absorbance of the resulting solution was measured at 540 nm. Ascorbic acid was used as the standard reference compound for comparison.

Cellular and Nuclear Morphology

Approximately 5 × 10^3 cells were coated onto L-lysine (Sigma)-coated coverslips and allowed to adhere overnight. The cells were then exposed to IC_{50} concentrations of the extract for 24 hours. After treatment, the cells were gently washed and fixed using 4% paraformaldehyde (PFA), followed by another wash with chilled phosphate-buffered saline (PBS). Nuclear staining was performed using Hoechst 33258 (Sigma) at a concentration of 2 µg/mL for 2 minutes at room temperature. Subsequently, the cells were rinsed again with PBS and mounted using a PBS: glycerol mixture (1:9) containing propyl gall ate for microscopic observation.

Apoptosis Assay (Annexing V-FITC/PI Double Staining)

Approximately 5 × 10^5 cells were seeded in T-25 culture flasks and allowed to grow overnight. The cells were then treated with IC_{50} concentrations of the extract for a duration of 24 hours. Following treatment, the cells were collected, washed with phosphate-buffered saline (PBS), and stained with Annexing V-FITC and Propidium iodide for 15 minutes in the dark, as per the manufacturer's instructions (BD Biosciences). The stained cells were subsequently analysed using flow cytometer (BD FACSVerse) to assess apoptotic activity.

Cell Cycle Analysis

Approximately 5 × 10^5 cells were seeded in T-25 flasks and incubated overnight to allow proper attachment and growth. The cells were then exposed to IC_{50} concentrations of the extract for 24 hours. (Upreti S, *et* al., 2024) [37]. After treatment, the cells were collected and washed with phosphate-buffered saline (PBS), followed by fixation in 70% ethanol. The fixed cells were subsequently treated with RNA at 37°C for 2 hours to remove RNA, and then stained with Propidium iodide (PI). The samples were incubated in the dark for 15 minutes and finally analysed using flow cytometer to evaluate changes in cell cycle distribution.

Gene Expression Analysis by Semi-Quantitative RT-PCR

Following 24 hours of treatment with IC_{50} concentrations, the cells were collected and washed with phosphate-buffered saline (PBS). Total RNA was extracted using Tri-reagent (Sigma) according to the manufacturer's instructions. The quality of the isolated RNA was verified using a bleach gel method, and its quantity was determined through UV spectrophotometry. Complementary DNA (cDNA) was synthesized from 1 µg of RNA using a first-strand cDNA synthesis kit (Thermo Scientific) as per the provided protocol. Subsequently, 1 µL of the synthesized cDNA was used as a template for PCR amplification of selected apoptotic genes, with GAPDH serving as the internal control. (Venkatesan U, Muniyan R. *et al*., 2024). Primers were designed using Primer3 software, and the corresponding sequences along with PCR conditions are provided in Table 1. The amplified PCR products were separated on 2% agarose gels and visualized using a gel documentation system (UVP MultiDoc-It). Densitometry analysis was performed using NIH Image software to determine the relative expression levels of genes compared to untreated control samples.

Protein Expression Analysis by immune blotting

Total cellular proteins were extracted from treated cells using 1× sample loading buffer. Equal amounts of protein (50 µg per sample) were separated on 10% or 12% polyacrylamide gels through electrophoresis. The resolved proteins were then transferred onto nitrocellulose membranes (Pall, 0.22 µm pore size) and blocked with 5% bovine serum albumin (BSA) for 3 hours at room temperature to prevent non-specific binding. The membranes were subsequently incubated overnight at 4°C with primary antibodies under gentle agitation. After incubation, the blots were washed with TBS-T (Tris-buffered saline containing 0.05% Tween 20) and then treated with alkaline phosphatase (AP)-conjugated secondary antibodies for 3 hours at room temperature. Following additional washes with TBS-T and TBS, the membranes were developed using NBT-BCIP substrate (Sigma) until visible protein bands appeared. (Venkatesan U, *et al.,* 2026) [38]. The reaction was then terminated using water, and the membranes were documented using a gel documentation system (UVP MultiDoc-It). Details regarding the antibodies and their respective dilutions are provided in Table 2.

Reactive Oxygen Species (ROS) Generation

Following a short treatment period of 3 hours, the cells were incubated with H_2DCFDA (Abcam) for 30 minutes at 37°C to detect intracellular reactive oxygen species. (Westphalia D*, et* al., 2024). After staining, the cells were washed with phosphate-buffered saline (PBS) to remove excess dye and then examined under an Epic-fluorescence microscope (Leica) to visualize ROS production.

Assessment of Mitochondrial Membrane Potential Loss

After 4 hours of treatment, the cells were stained with JC-1 dye (BD Biosciences) for 15 minutes at 37°C to evaluate changes in mitochondrial membrane potential. Following staining, the cells were washed with phosphate-buffered saline (PBS) to remove excess dye and then observed under an Epic-fluorescence microscope (Leica) for analysis.

ROS-Mediated DNA Damage

Detection of γH2AX Incorporation

To evaluate DNA damage induced by reactive oxygen species, γH2AX incorporation was analysed after 6 hours of

treatment. The cells were fixed with 4% paraformaldehyde (PFA) at room temperature for 15 minutes, followed by washing with phosphate-buffered saline (PBS). The fixed cells were then incubated overnight at 4°C with anti-γH2AX primary antibody (Cell Signalling Technology) in a humidified chamber. After incubation, the cells were washed with PBS and further incubated with a FITC-conjugated secondary antibody for 3 hours at room temperature. The samples were again washed with PBS, mounted using a PBS: glycerol mixture (1:9) containing propyl gall ate, and observed under an Epi-fluorescence microscope (Leica). Details regarding antibody specifications and dilutions are provided in Table 2.

Western Blot Analysis of DNA Damage-Responsive Proteins

Western blot analysis of proteins involved in the DNA damage response was carried out following the procedure described in the previous section. The specific antibodies used and their corresponding dilutions are listed in Table 2.

Statistical Analysis

All experiments were conducted in triplicate to ensure reliability of the results. The mean values and standard deviations (SD) were calculated using Microsoft Excel. Graphs and charts were generated with the help of Microsoft Excel and GraphPad Prism 5. Statistical analyses, including ANOVA and Student's t-test, were performed using GraphPad Prism 5 software.

Result

Cellular and Nuclear Morphology

Significant alterations in both cellular and nuclear morphology were observed in all treated cell groups. The treated cells exhibited typical features associated with apoptosis, including cell membrane shrinkage and the formation of cytoplasmic blebs. Additionally, Hoechst 33258 staining revealed clear chromatin condensation and nuclear fragmentation, confirming apoptotic changes (Fig 1, 2, and 3).

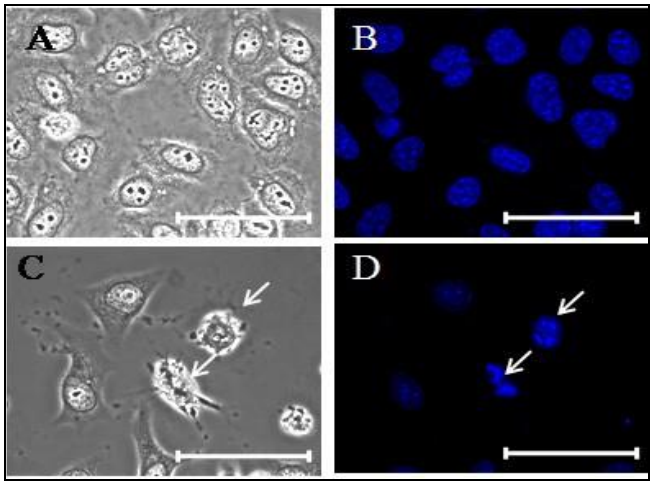

Fig 1: Effect of HIC fraction on cellular and nuclear morphology of HeLa cells. Arrows show apoptotic features. Scale represents 50 µm. A & B: Phase and fluorescent pictures of control cells. C & D: Phase and fluorescent pictures of treated cells.

Apoptosis Assay (Annexing V-FITC/PI Double Staining)

In HeLa cells, the control group showed 10.54% apoptotic cells, whereas treatment with HIC resulted in a significant increase to 46.52%, representing a 4.41-fold rise (Fig 4). Similarly, in SiHa cells, 16.01% apoptosis was observed in the control group, which increased to 42.26% following HIC treatment, indicating a 2.64-fold enhancement (Fig 5). In C33A cells, apoptosis increased markedly from 7.73% in the control group to 76.65% in treated cells, corresponding to a 9.92-fold increase (Fig 6).

Cell cycle shift

With HIC treatment, two types of responses were found in the cell lines. In HeLa and C33A cell lines, sub G0 population was increased suggesting cytotoxicity whereas, in SiHa cells, G1/S block was observed. In HeLa cells, G0G1 decreased by 3.66% with 8.64% increase in subG0 population C33A cells showed similar effect with 18.62% decrease in G0G1 and increase of 15.22% in sub G0 population. But in SiHa cells, G0G1 population was increased significantly by 4.65%.

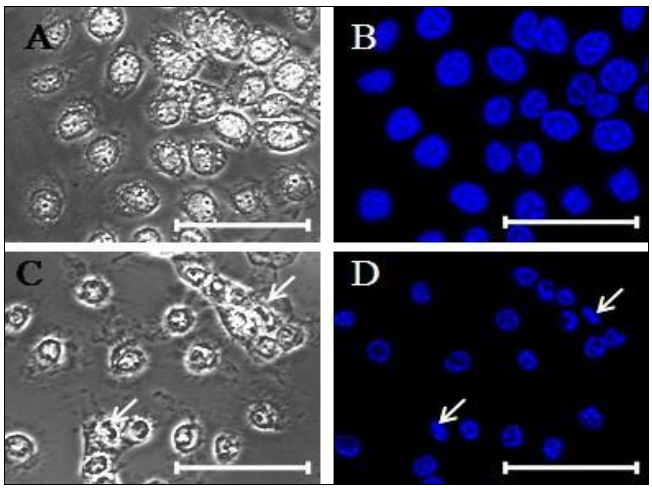

Fig 2: Effect of HIC fraction on cellular and nuclear morphology of SiHa cells. Arrows show apoptotic features. Scale represents 50 µm. A & B: Phase and fluorescent pictures of control cells. C & D: Phase and fluorescent pictures of treated cells.

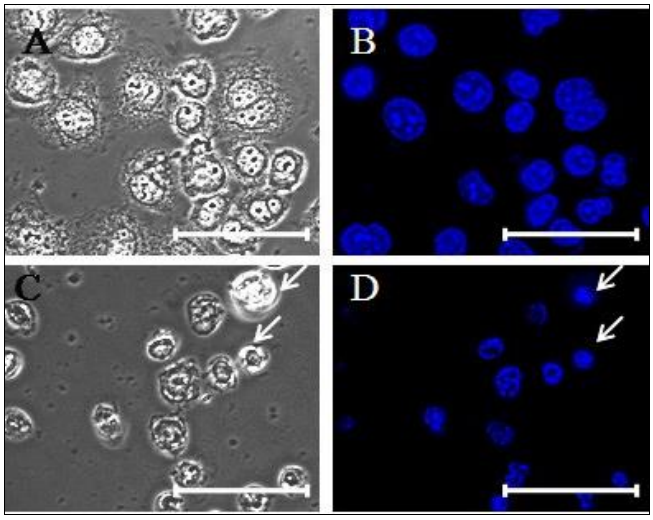

Fig 3: Effect of HIC fraction on cellular and nuclear morphology of C33A cells. Arrows show apoptotic features. Scale represents 50 µm. A & B: Phase and fluorescent pictures of control cells. C & D: Phase and fluorescent pictures of treated cells.

Cell Cycle Analysis

Treatment with HIC resulted in two distinct patterns of cell cycle response across the studied cell lines. In HeLa and

C33A cells, there was a notable increase in the sub-G0 population, indicating enhanced cytotoxicity. Specifically, HeLa cells showed a 3.66% reduction in the G0/G1 phase along with an 8.64% rise in the sub-G0 population (Fig 7). Similarly, C33A cells exhibited an 18.62% decrease in the G0/G1 phase and a corresponding 15.22% increase in the sub-G0 population (Fig 9). In contrast, SiHa cells demonstrated a different response, with a significant increase of 4.65% in the G0/G1 phase, suggesting a G1/S phase arrest (Fig 8).

Gene Expression Study

The gene expression analysis demonstrated significant alterations in the expression patterns of multiple genes. There was an up regulation of pro-apoptotic genes, while genes associated with anti-apoptotic functions, cell proliferation, and viral oncogenic activity were down regulated. In HeLa cells, the expression levels of Bcl-2, ET-1, and HPV-18 E6 were reduced by 0.33-fold, 0.12-fold, and 0.63-fold, respectively. Conversely, p53 expression showed a marked increase of 0.93-fold, while BAX and p21 levels were elevated by 0.34-fold and 0.008-fold, respectively (Fig 10). In SiHa cells, a substantial decrease in Bcl-2 expression (0.87-fold) was observed, along with slight reductions in ET-1 and HPV-16 E6 expression (0.1-fold and 0.11-fold, respectively). In contrast, BAX expression increased significantly by 0.77-fold, with moderate increases in p53 (0.36-fold) and p21 (0.13-fold) (Fig 11). In C33A cells, Bcl-2 expression decreased by 0.15-fold, whereas BAX, p53, and p21 expressions were elevated by 1.09-fold, 1.9-fold, and 1.25-fold, respectively (Fig 12). As expected, ET-1 expression was absent in C33A cells, which lack HPV infection, since this gene is typically associated with HPV-positive cell lines.

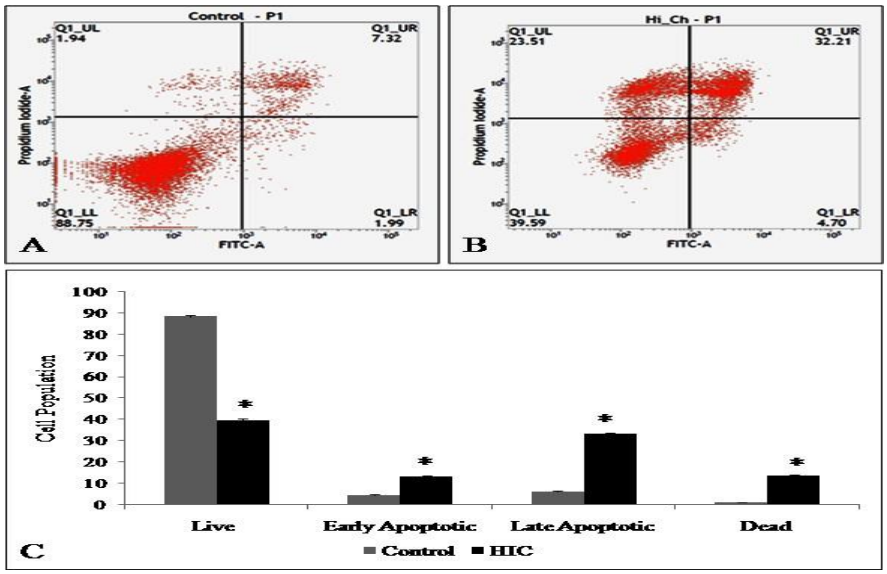

Fig 4: Representative dot plots [A) Control, B) HIC] along with Bar graph [C] showing cell distribution in different sets of HeLa cells after Annexing V-FITC/PI staining; columns represent the cell populations while bars represent standard deviations. * denotes significant difference between control and treated sets ($P < 0.05$) [T-Test-GraphPad Prism5].

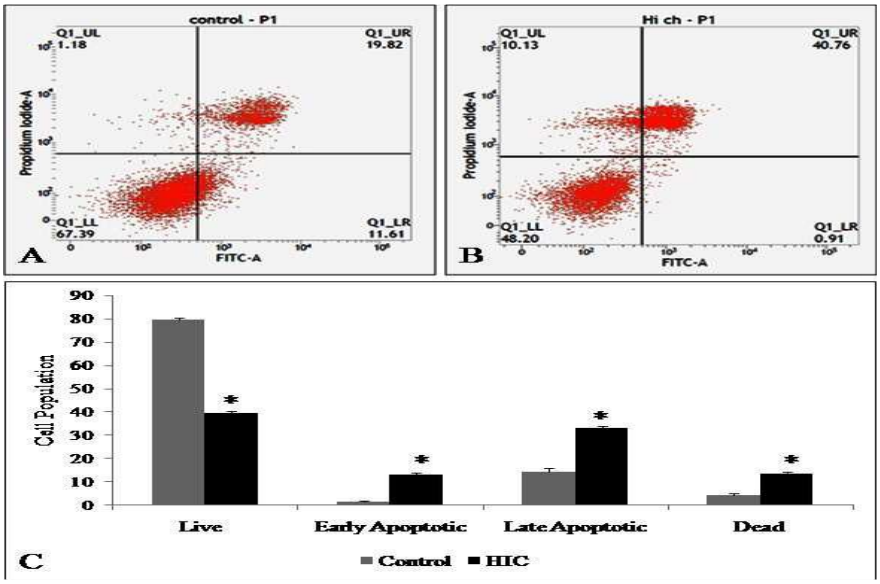

Fig 5: Representative dot plots [A) Control, B) HIC] along with Bar graph [C] showing cell distribution in different sets of SiHa cells after Annexing V-FITC/PI staining; columns represent the cell populations while bars represent standard deviations. * denotes significant difference between control and treated sets ($P < 0.05$) [T-Test- GraphPad Prism5

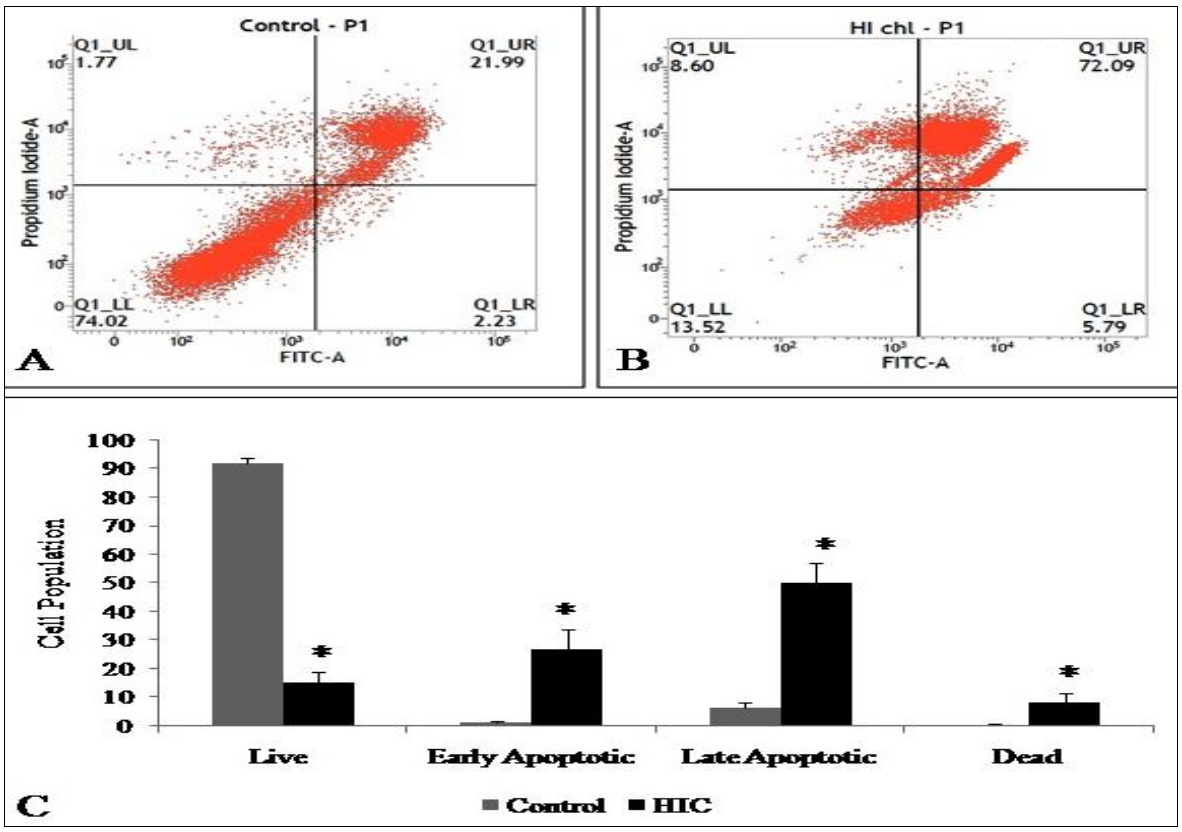

Fig 6: Representative dot plots [A) Control, B) HIC] along with Bar graph [C] showing cell distribution in different sets of C33A cells after Annexing V-FITC/PI staining; columns represent the cell populations while bars represent standard deviations. * denotes significant difference between control and treated sets ($P < 0.05$) [T-Test-GraphPad Prism5].

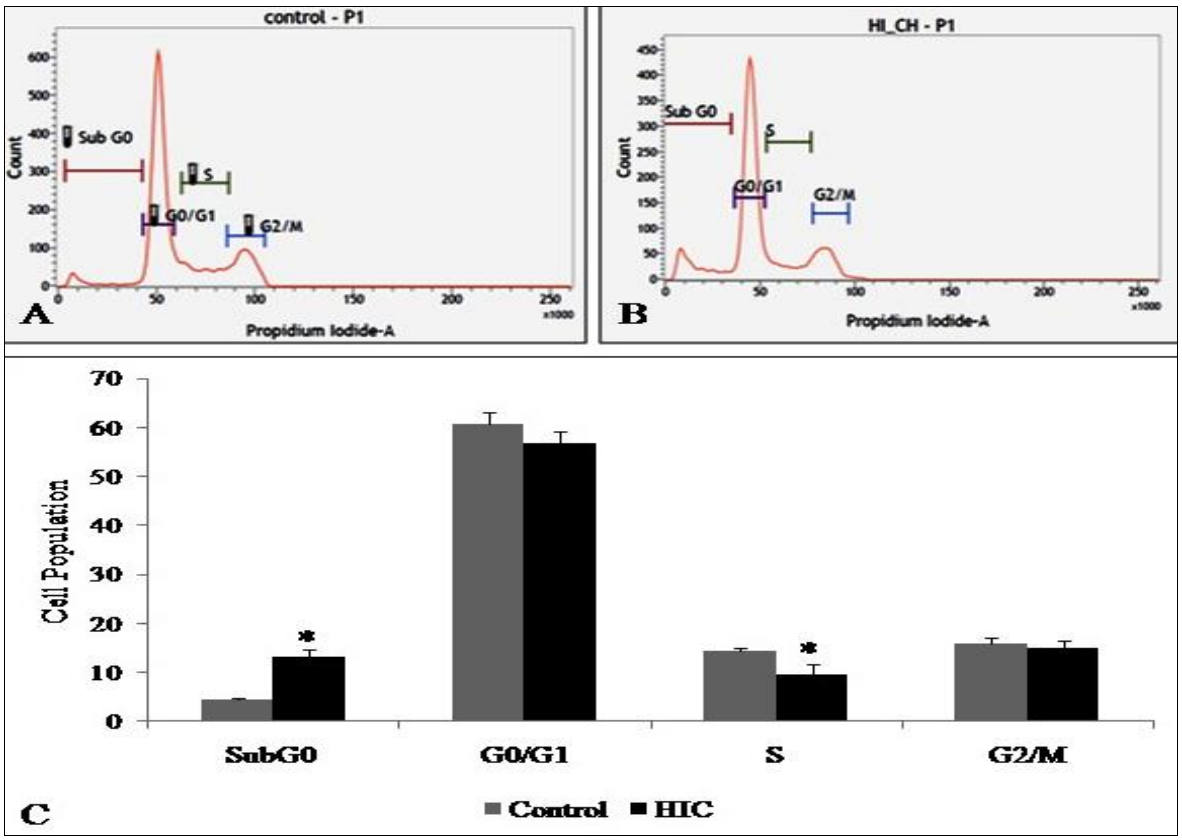

Fig 7: Representative histograms [A) Control, B) HIC] along with Bar graph [C] showing cell distribution in different phases in sets of HeLa cells; columns represent the cell populations while bars represent standard deviations. * denotes significant difference between control and treated sets ($P < 0.05$) [T-Test-GraphPad Prism

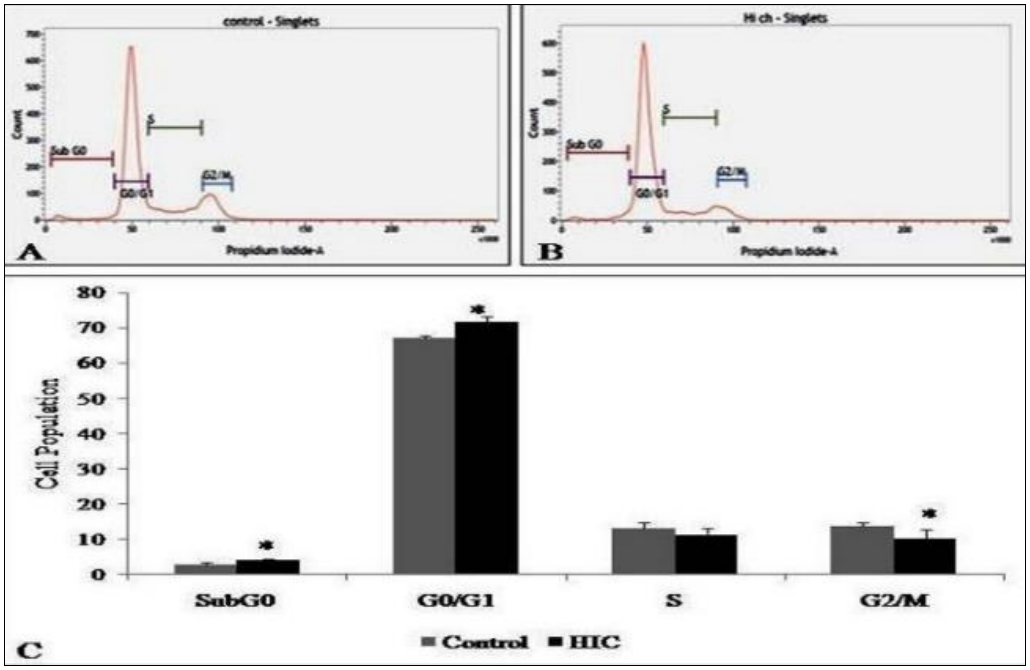

Fig 8: Representative histograms [A) Control, B) HIC] along with Bar graph [C] showing cell distribution in different phases in sets of SiHa cells; columns represent the cell populations while bars represent standard deviations. * denotes significant difference between control and treated sets ($P < 0.05$) [T-Test-GraphPad Prism5].

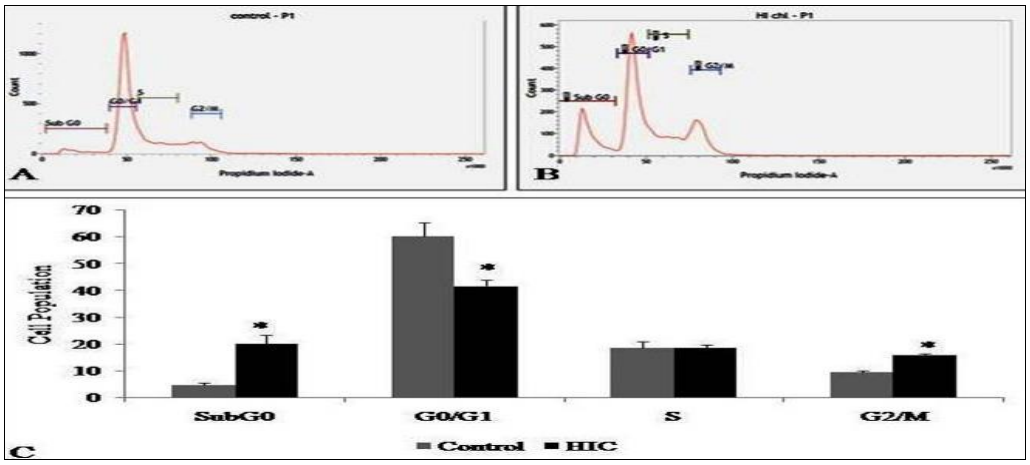

Fig 9: Representative histograms [A) Control, B) HIC] along with Bar graph [C] showing cell distribution in different phases in sets of C33A cells; columns represent the cell populations while bars represent standard deviations. * denotes significant difference between control and treated sets ($P < 0.05$) [T-Test-GraphPad Prism5].

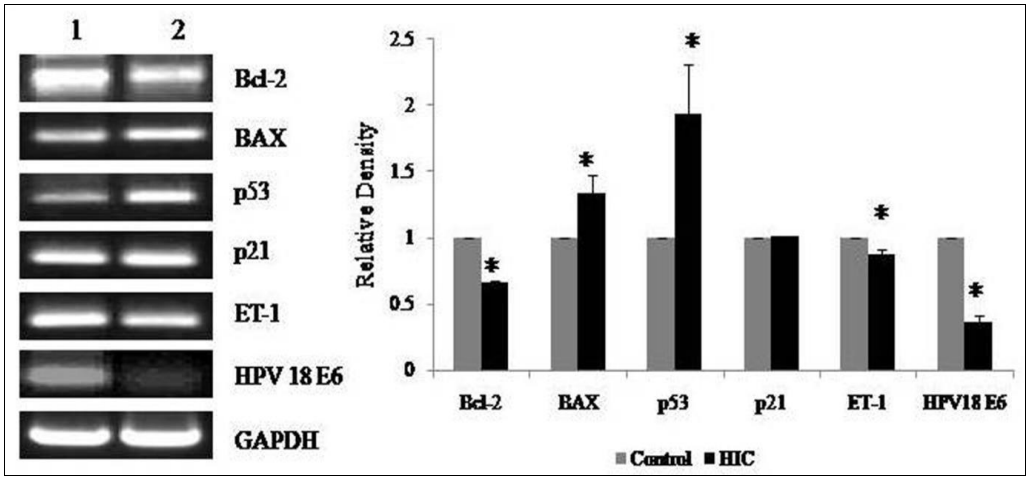

Fig 10: Representative PCR expressions of several genes in control and treated sets in HeLa cells [1: Control set, 2: HIC treated] along with densitometry analysis, columns represent the relative densities while bars represent standard deviations. * denotes significant difference between control and treated sets ($P < 0.05$) [T-Test-GraphPad Prism5].

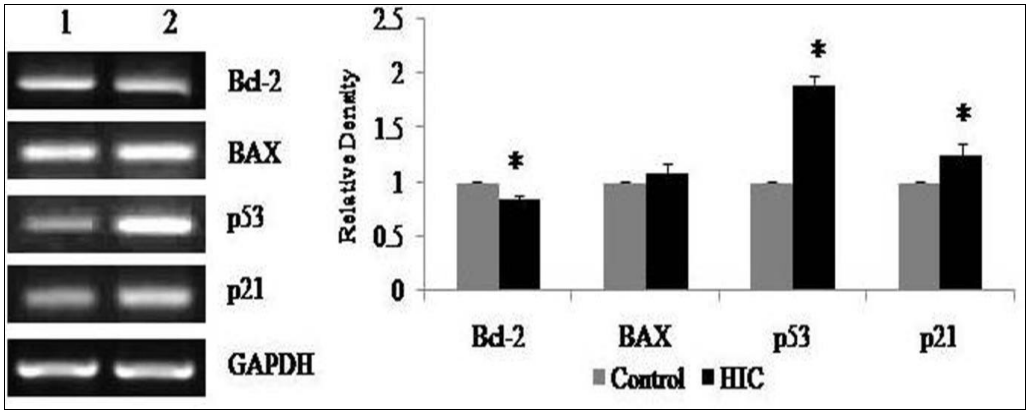

Fig 11: Representative PCR expressions of several genes in control and treated sets in SiHa cells [1: Control set, 2: HIC treated] along with densitometry analysis, columns represent the relative densities while bars represent standard deviations. * denotes significant difference between control and treated sets ($P < 0.05$) [T-Test-GraphPad Prism5].

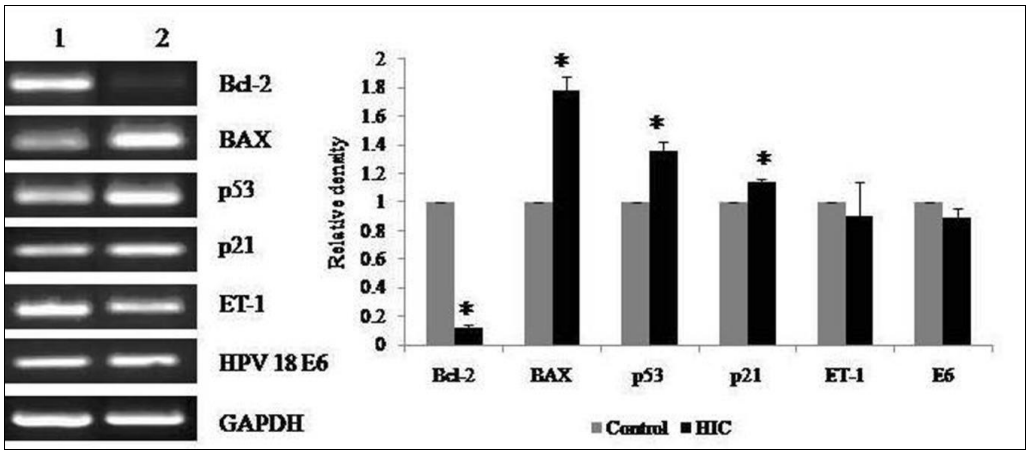

Fig 12: Representative PCR expressions of several genes in control and treated sets in C33A cells [1: Control set, 2: HIC treated] along with densitometry analysis, columns represent the relative densities while bars represent standard deviations. * denotes significant difference between control and treated sets ($P < 0.05$) [T-Test-GraphPad Prism5].

Protein Expression Study

Protein expression analysis revealed that treatment led to increased levels of key apoptotic markers, including cleaved caspase-3, BAX, p53, and p21, while the expression of anti-apoptotic Bcl-2 and viral on co-proteins (HPV 16/18 E6) was reduced across all cell lines. In HeLa cells, Bcl-2 expression decreased by 0.21-fold and HPV-18 E6 by 0.73-fold. In contrast, the levels of cleaved caspase-3, BAX, p53, and p21 increased by 5.017-fold, 1.51-fold, 1.03-fold, and 1.84-fold, respectively (Fig 13). In SiHa cells, cleaved caspase-3 expression rose by 1.64-fold, while BAX, p53, and p21 levels increased by 1.5-fold, 1.52-fold, and 1.47-fold, respectively. Meanwhile, Bcl-2 and HPV-16 E6 expressions decreased by 0.17-fold and 0.62-fold (Fig 14). In C33A cells, a substantial increase was observed in cleaved caspase-3 (6.31-fold), BAX (2.06-fold), p53 (1.25-fold), and p21 (3.65-fold), accompanied by a decrease in Bcl-2 expression by 0.18-fold (Fig 15).

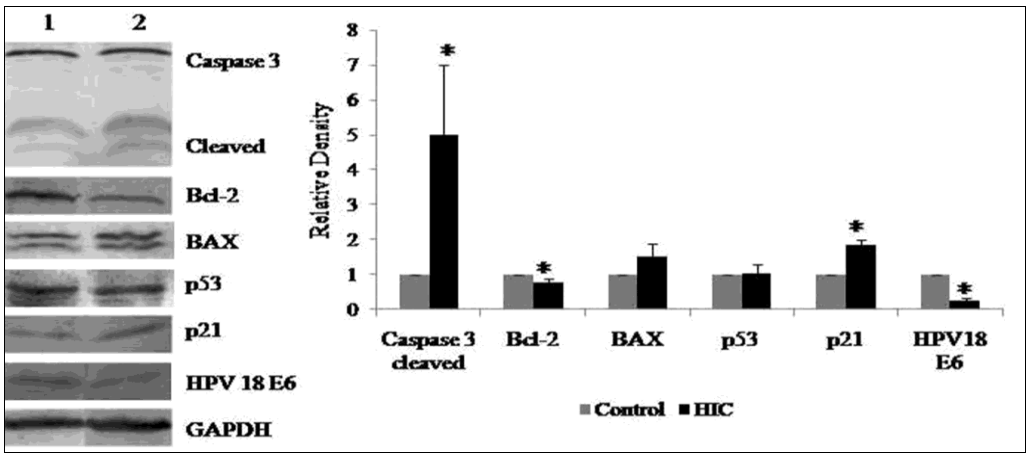

Fig 13: Representative western blots of several genes in control and treated sets in HeLa cells [1: Control set, 2: HIC treated] along with densitometry analysis, columns represent the relative densities while bars represent standard deviations. * denotes significant difference between control and treated sets ($P < 0.05$)

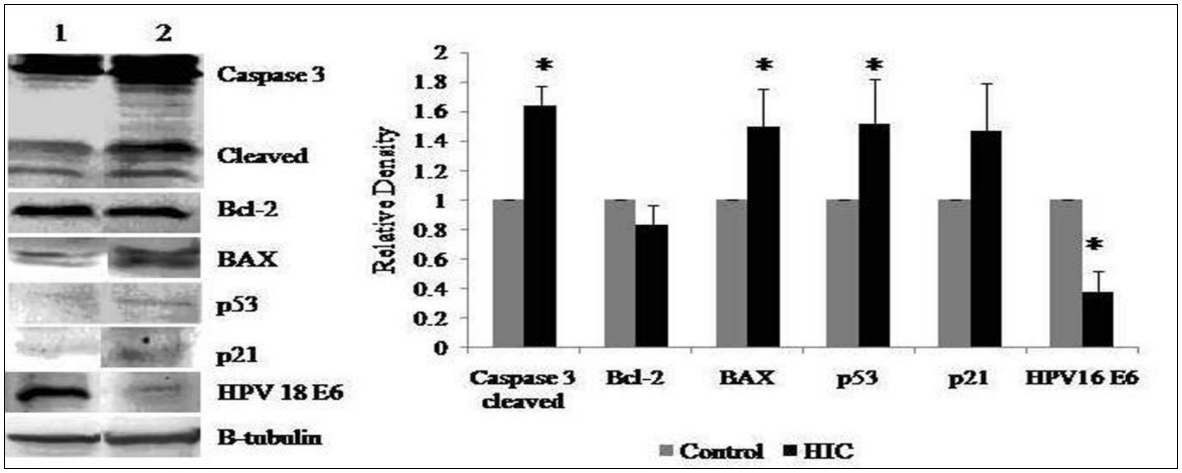

Fig 14: Representative western blots of several genes in control and treated sets in SiHa cells [1: Control set, 2: HIC treated] along with densitometry analysis, columns represent the relative densities while bars represent standard deviations. * denotes significant difference between control and treated sets ($P < 0.05$) [T-Test-GraphPad Prism5].

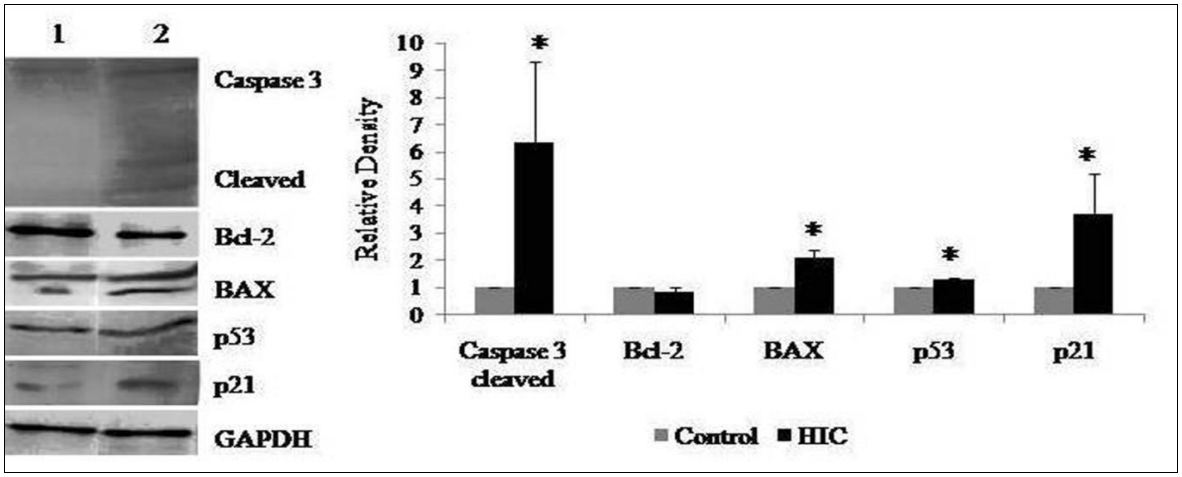

Fig 15: Representative western blots of several genes in control and treated sets in C33A cells [1: Control set, 2: HIC treated] along with densitometry analysis, columns represent the relative densities while bars represent standard deviations. * denotes significant difference between control and treated sets ($P < 0.05$) [T-Test-GraphPad Prism5].

ROS generation by HIC treatment

In the presence of reactive oxygen species (ROS), H_2DCFDA is oxidized to form the fluorescent compound DCF, which emits green fluorescence. No detectable fluorescence was observed in untreated cells, indicating minimal ROS production. However, treated cells showed a strong increase in green fluorescence, reflecting elevated ROS levels across all cell lines (Fig 16, 17, and 18). The percentage of ROS-positive cells was found to be 84.27%, 83.27%, and 81.98%, respectively.

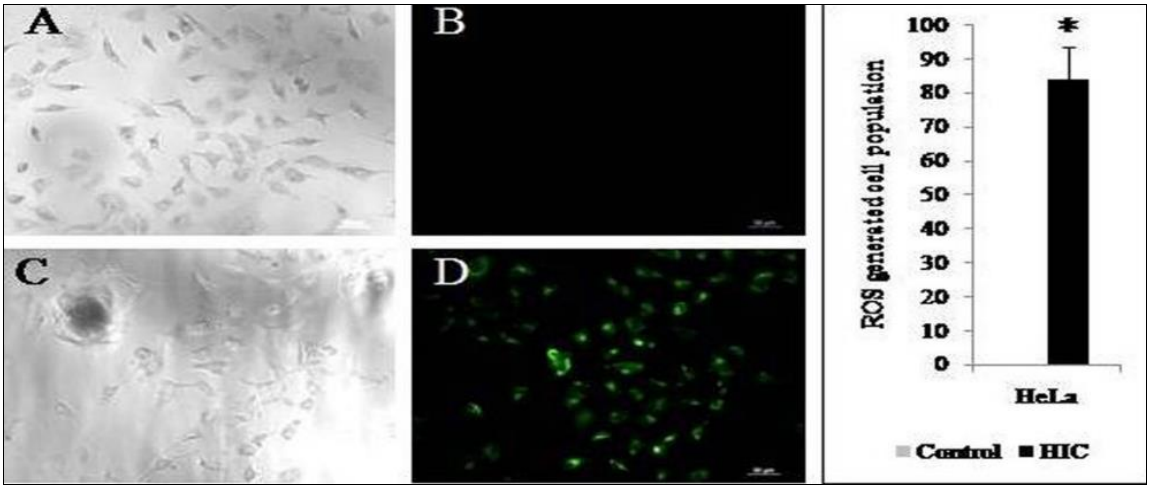

Fig 16: ROS formation in HeLa cells. Green fluorescence showed the presence of DCF. Scale represents 50 µm. A & B: Control cells, C & D: Treated cells along with bar diagram showing ROS generated cell population. Columns represent the cell populations while bars represent standard deviations. * denotes significant difference between control and treated sets ($P < 0.05$) [T-Test-GraphPad Prism5].

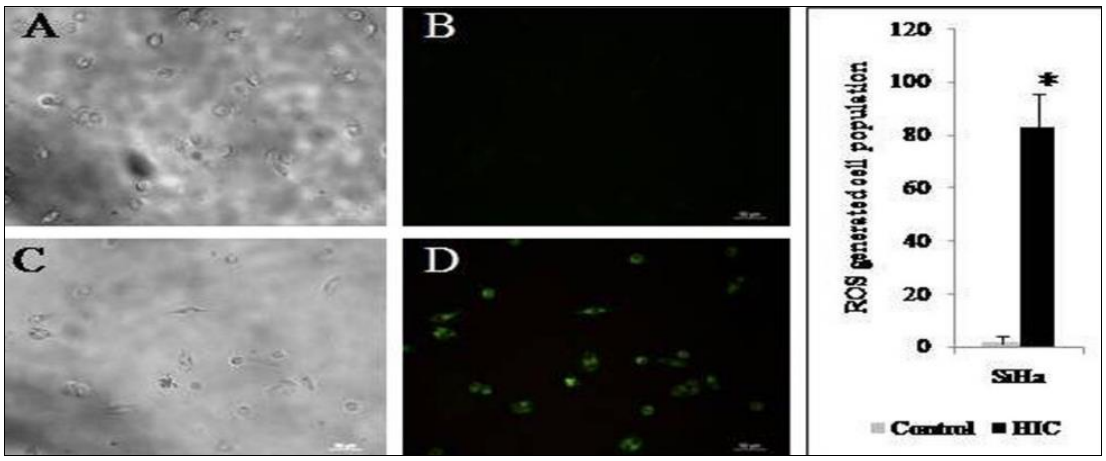

Fig 17: ROS formation in SiHa cells. Green fluorescence showed the presence of DCF. Scale represents 50 µm. A & B: Control cells, C & D: Treated cells along with bar diagram showing ROS generated cell population. Columns represent the cell populations while bars represent standard deviations. * denotes significant difference between control and treated sets ($P < 0.05$) [T-Test-GraphPad Prism5].

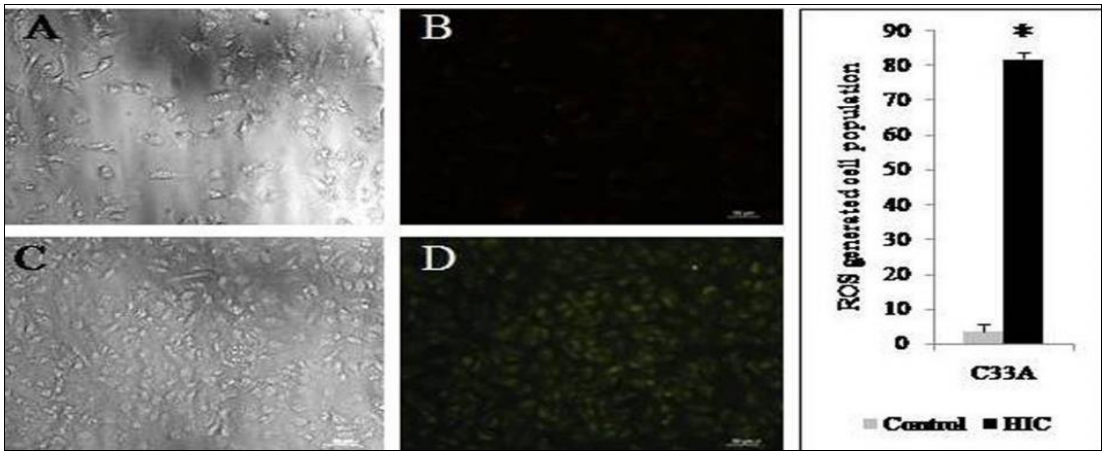

Fig 18: ROS formation in C33A cells. Green fluorescence showed the presence of DCF. Scale represents 50 µm. A & B: Control cells, C & D: Treated cells along with bar diagram showing ROS generated cell population. Columns represent the cell populations while bars represent standard deviations. * denotes significant difference between control and treated sets ($P < 0.05$) [T-Test-GraphPad Prism5]

Mitochondrial Membrane Potential (MMP) Loss Induced by HIC Treatment

The generation of reactive oxygen species (ROS) can lead to disruption of mitochondrial membrane potential. JC-1 dye exhibits red fluorescence when present in its aggregated form within healthy mitochondria, whereas it emits green fluorescence in its monomeric form in depolarized or damaged mitochondria. In treated cells, a marked increase in green fluorescence was observed, indicating significant loss of mitochondrial membrane potential. The percentage of depolarized cells was recorded as 70.01% in HeLa, 79.54% in SiHa, and 87.76% in C33A cells (Fig 19, 20, and 21).

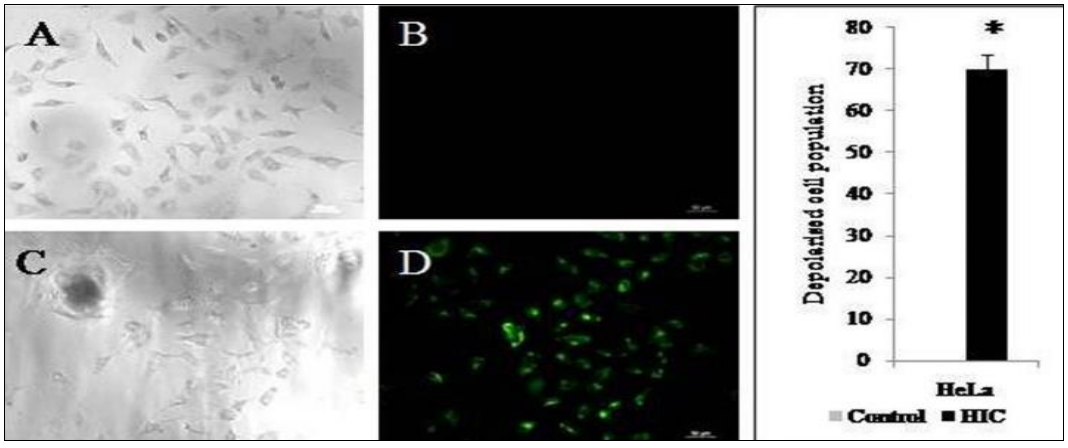

Fig 19: Loss of MMP in HeLa cells. Green fluorescence showed the presence of JC1 monomers in depolarized cells. Scale represents 50 µm. A & B: Control cells, C & D: Treated cells along with bar diagram showing depolarized cell population. Columns represent the cell populations while bars represent standard deviations. * denotes significant difference between control and treated sets ($P < 0.05$) [T-Test-GraphPad Prism5].

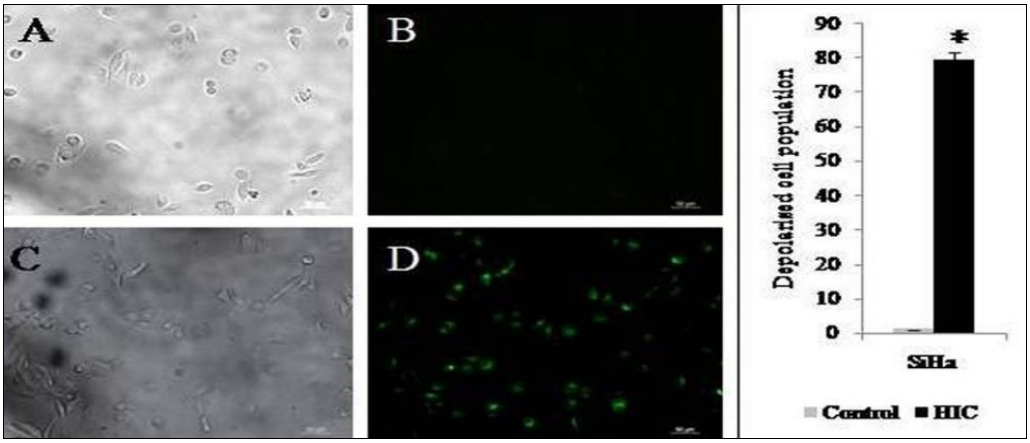

Fig 20: Loss of MMP in SiHa cells. Green fluorescence showed the presence of JC1 monomers in depolarized cells. Scale represents 50 µm. A & B: Control cells, C & D: Treated cells along with bar diagram showing depolarized cell population. Columns represent the cell populations while bars represent standard deviations. * denotes significant difference between control and treated sets ($P < 0.05$) [T-Test-GraphPad Prism5].

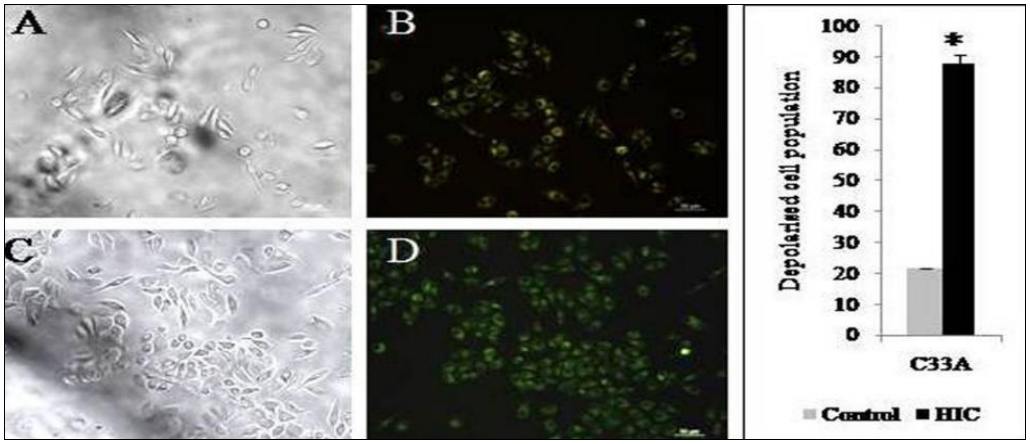

Fig 21: Loss of MMP in C33A cells. Green fluorescence showed the presence of JC1 monomers in depolarized cells. Scale represents 50 µm. A & B: Control cells, C & D: Treated cells along with bar diagram showing depolarized cell population. Columns represent the cell populations while bars represent standard deviations. * denotes significant difference between control and treated sets ($P < 0.05$) [T-Test-GraphPad Prism5].

Incorporation of γH2AX

In all three cell lines, treated samples exhibited clear γ-H2AX signals, which serve as an indicator of DNA damage. At the 6-hour time point, the presence of this phosphorylated form of H2AX confirmed the occurrence of DNA damage. This damage is likely responsible for triggering apoptotic pathways in the treated cells (Fig 22, 23, and 24).

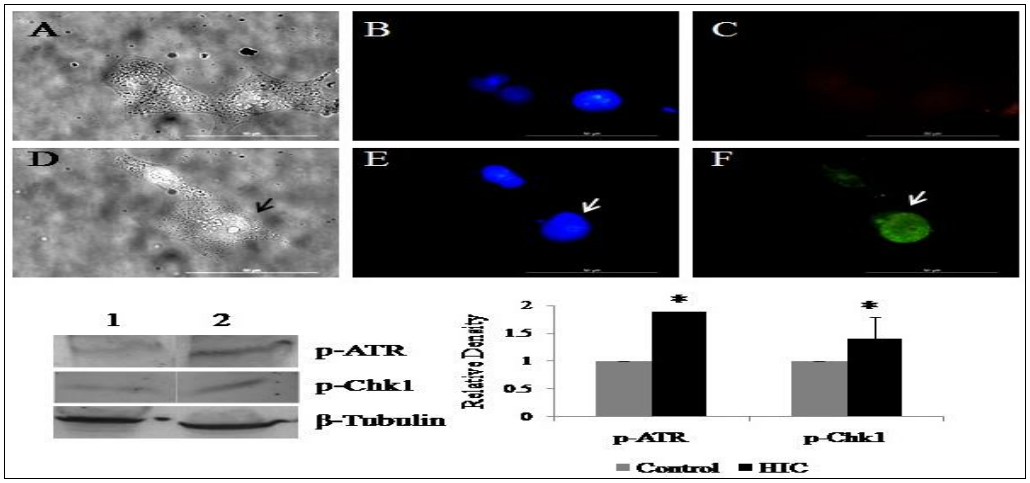

Fig 22: DNA damage responses in HeLa cells. ΓH2AX incorporation [A, B & C: Phase, Hoechst 33258 and γH2AX-FITC in control cells; D, E, and F: Phase, Hoechst 33258 and γH2AX-FITC in treated cells. Representative western blots of several genes in control and treated sets [1: Control set, 2: HIC treated] along with densitometry analysis, columns represent the relative densities while bars represent standard deviations. * denotes significant difference between control and treated sets ($P < 0.05$) [T-Test-GraphPad Prism5].

Western Blot Analysis of DNA Damage-Responsive Proteins

The expression levels of important proteins involved in DNA damage response pathways were analysed. Across all cell lines, phosphorylated ATM (p-ATM) and phosphorylated Chk2 (p-Chk2) were not detected. However, the presence of phosphorylated ATR (p-ATR) and phosphorylated Chk1 (p-Chk1) was observed, indicating the occurrence of single-strand DNA damage. In HeLa cells, p-ATR and p-Chk1 expression levels increased by 1.88-fold and 1.41-fold, respectively (Fig 22). In SiHa cells, a higher increase was noted, with p-ATR and p-Chk1 levels rising by 2.21-fold and 1.95-fold, respectively (Fig 23). A similar trend was observed in C33A cells, where p-ATR and p-Chk1 expressions increased by 2.96-fold and 1.56-fold, respectively (Fig 24).

GC–MS Analysis

The GC–MS analysis revealed the presence of various phytochemicals, including phenolic compounds and terpenoids, with squalling being one of the components identified. Squalling is known to function as a precursor in steroid biosynthesis. The major compounds detected a LC–MS Analysis. The LC–MS analysis indicated the presence of various phytochemical constituents, including phenolic compounds and alkaloids. The peaks identified in the analysis are summarized in Table 4, while the LC–MS chromatogram is illustrated in Fig 26.

Column Chromatography and GC–MS Analysis

Approximately 25 sub fractions were obtained from the HIC fraction using silica gel column chromatography. Among these, sub fractions 6, 7, 8, 9, and 10 exhibited notable cytotoxic activity as determined by the MTT assay. These active fractions were further analysed using GC–MS, and several common phytochemical constituents were identified through comparison with the NIST library. The major compounds detected included fatty acid derivatives such as palmitic acid TMS ester, stearic acid TMS ester, and linoleic acid TMS ester. Specifically, sub fraction 6 contained 31.2% palmitic acid TMS ester, 11.6% linoleic acid TMS ester, 8.7% oleic acid TMS ester, and 37.6% stearic acid TMS ester. sub fraction 7 consisted of 1.1% benzoic acid TMS ester, 0.9% phenol-2,4-bis(1,1-dimethylethyl), 22.7% palmitic acid TMS ester, 1.06% linoleic acid TMS ester, and 13.5% stearic acid TMS ester. Sub fraction 8 showed 1.68% benzoic acid TMS ester, 24.2% palmitic acid TMS ester, and 34.6% stearic acid TMS ester. In sub fraction 9, 1.21% benzenacetic acid TMS ester, 4.8% benzoic acid TMS ester, 26.2% palmitic acid TMS ester, and 37.17% stearic acid TMS ester were identified. Sub fraction 10 contained 5.08% azelaic acid-bis TMS ester, 36.17% palmitic acid TMS ester, and 44.08% stearic acid TMS ester.

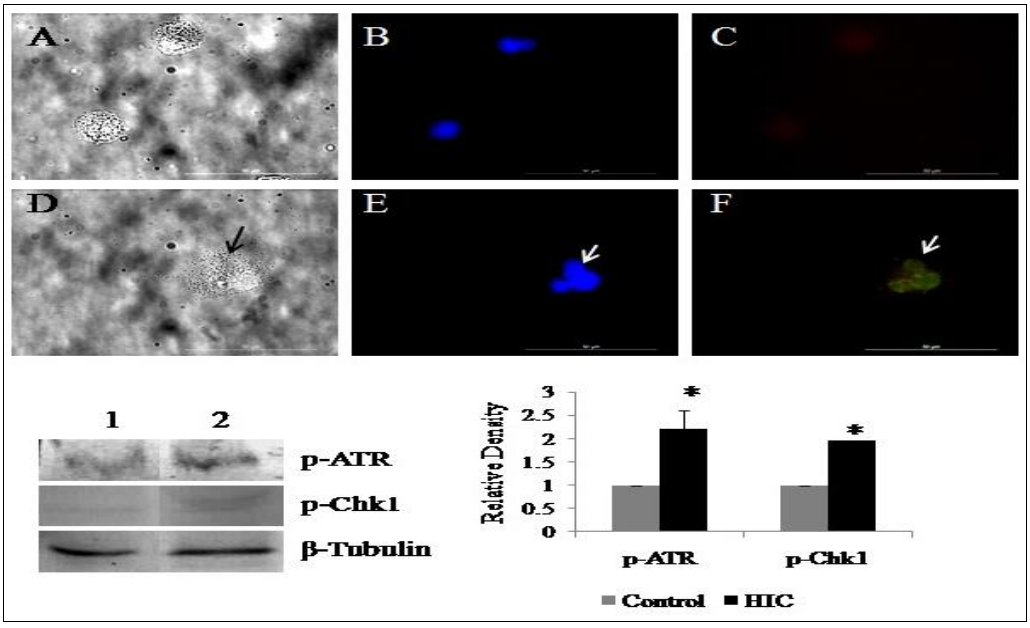

Fig 23: DNA damage responses in SiHa cells. ΓH2AX incorporation [A, B & C: Phase, Hoechst 33258 and γH2AX-FITC in control cells; D, E, and F: Phase, Hoechst 33258 and γH2AX-FITC in treated cells. Representative western blots of several genes in control and treated sets [1: Control set, 2: HIC treated] along with densitometry analysis, columns represent the relative densities while bars represent standard deviations. * denotes significant difference between control and treated sets ($P < 0.05$) [T-Test-GraphPad Prism5].

Table 3: GC-MS analysis of *Acalypha. Indica* chloroform fraction (HIC)

RT	Area %	Probable compound
18.15	22.618	Phenol-2,4-bis-1,1-dimethylethyl
19.951	4.065	Cetane
24.330	7.274	E-15 Heptadecanal
25.963	1.015	Phthalic acid hex-3-yl isobutyl ester
26.888	2.336	1,2-Benzen dicarboxylic acid butyl ester
27.808	4.075	Dibutylphthalate
28.208	2.764	Phthalic acid butyl hex-3-yl ester
28.321	7.505	5-Icosene

29.622	1.068	Phthalic acid butyl-8-chlorooctylester
31.961	5.752	Cycloeicosene
34.914	2.227	1,3,4,5,6-tetra-tert-butylbiphenyldiol
35.307	2.909	1-Heniocosanol
37.773	8.654	Phthalic acid, di (2-propylpentyl) ester
42.477	8.384	Squalene

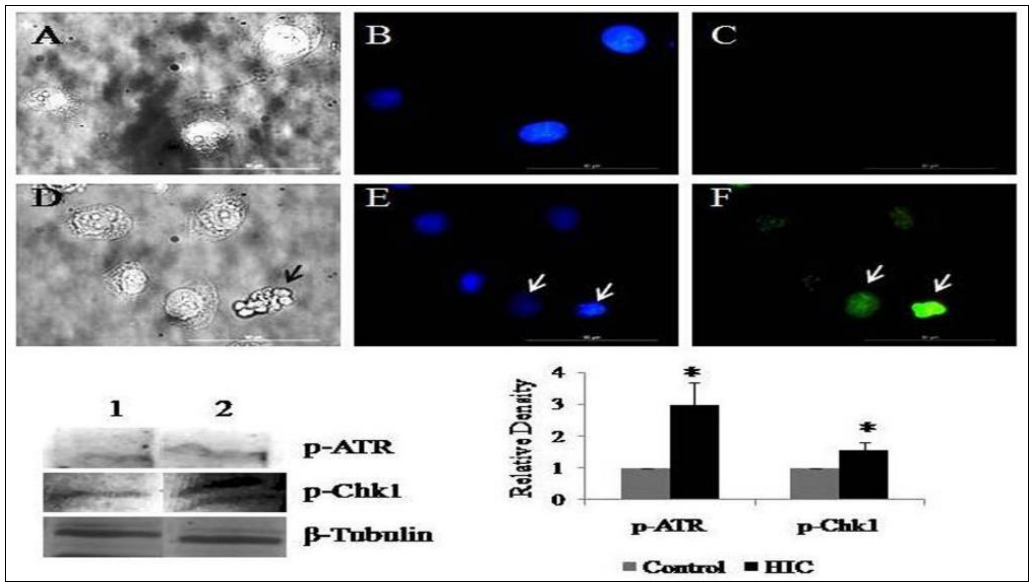

Fig 24: DNA damage responses in C33A cells. Γ-H2AX incorporation [A, B & C: Phase, Hoechst 33258 and γH2AX-FITC in control cells; D, E, and F: Phase, Hoechst 33258 and γH2AX-FITC in treated cells. Representative western blots of several genes in control and treated sets [1: Control set, 2: HIC treated] along with densitometry analysis, columns represent the relative densities while bars represent standard deviations. * denotes significant difference between control and treated sets ($P < 0.05$) [T-Test-GraphPad Prism5

Discussion

The elevated proportion of Annexing V-FITC-positive cells confirmed that the treatment effectively induced apoptotic cell death across all examined cell lines, with notable increases in both early and late apoptotic populations. In HeLa and C33A cells, HIC treatment led to an accumulation of cells in the sub-G0 phase, indicating cytotoxic effects, whereas in SiHa cells, a clear G1/S phase arrest was observed. The findings suggest that p21 plays a key role in regulating this cell cycle arrest, while p53 functions as a central regulator of the apoptotic pathway. A reduction in HPV 16/18 E6 expression in treated HeLa and SiHa cells likely contributed to the stabilization of p53, which in turn promoted p21 up regulation. Additionally, decreased levels of the anticrime growth factor ET-1 may have contributed to reduced cell proliferation in HPV-positive cell lines.

The observed increase in pro-apoptotic proteins such as cleaved caspase-3, Box, p53, and p21, along with a decrease in the anti-apoptotic protein Bcl-2, further supports the involvement of apoptosis as the primary mechanism of cell death. *In vitro* cytotoxicity is often linked to DNA damage, which can elevate p53 levels and subsequently induce p21 expression, leading to cell cycle arrest. In this study, HIC treatment triggered ROS generation within 3 hours, resulting in mitochondrial membrane potential loss and extensive DNA damage. The activation of DNA damage response pathways was confirmed by γH2AX incorporation and increased expression of p-ATR and p-Chk1. Severe DNA damage can disrupt mitochondrial integrity, promoting the release of cytochrome c and activation of capsizes, ultimately leading to apoptosis. The proposed mechanism of action of HIC treatment is illustrated in the hypothetical model presented in Fig 27.

GC–MS and LC–MS analyses of the HIC fraction revealed the presence of a wide range of bioactive phytochemicals, including alkaloids, phenolic compounds, terpenoids, and fatty acids. Notable constituents identified in the fraction included indicate N-oxide and heliotrope, along with other compounds such as ruin, catching, methoxy-cinnamic acid, squalling, and phenol-2,4-bis(1,1-dimethylethyl). Both short-chain fatty acids (e.g., butanedioic acid and benzoic acid derivatives) and long-chain fatty acids (e.g., stearic acid, oleic acid, and linoleic acid) were also detected. Several of these unsaturated fatty acids have been previously reported to exhibit anticancer properties.

Additionally, phenol-2, 4-bis (1, 1-dimethylethyl), identified in the HIC fraction, has been reported in bioactive fractions of *Solanum trilobatum* with inhibitory effects on Ehrlich's Ascites Carcinoma. Stearic acid, also present in the fraction, has been associated with inhibitory activity against cervical cancer cell lines such as HOG-1. Palmitic acid, detected in this study, has shown selective cytotoxic effects against MOLT-4 human leukemic cells, potentially through inhibition of DNA topoisomerase I. Linoleic acid has demonstrated inhibitory effects on rat hematoma (AH-109A) cells, while oleic acid has been reported to suppress tumour cell growth via calcium-dependent signalling pathways. Furthermore, various benzoic acid derivatives, including methyl-substituted forms and benzene acetic acid, were identified. Azelaic acid, another compound present in the fraction, is known for its selective cytotoxic effects against melanoma cells. These findings suggest that the observed biological activities of the HIC fraction may be attributed to the combined effects of these diverse phytochemical constituents.

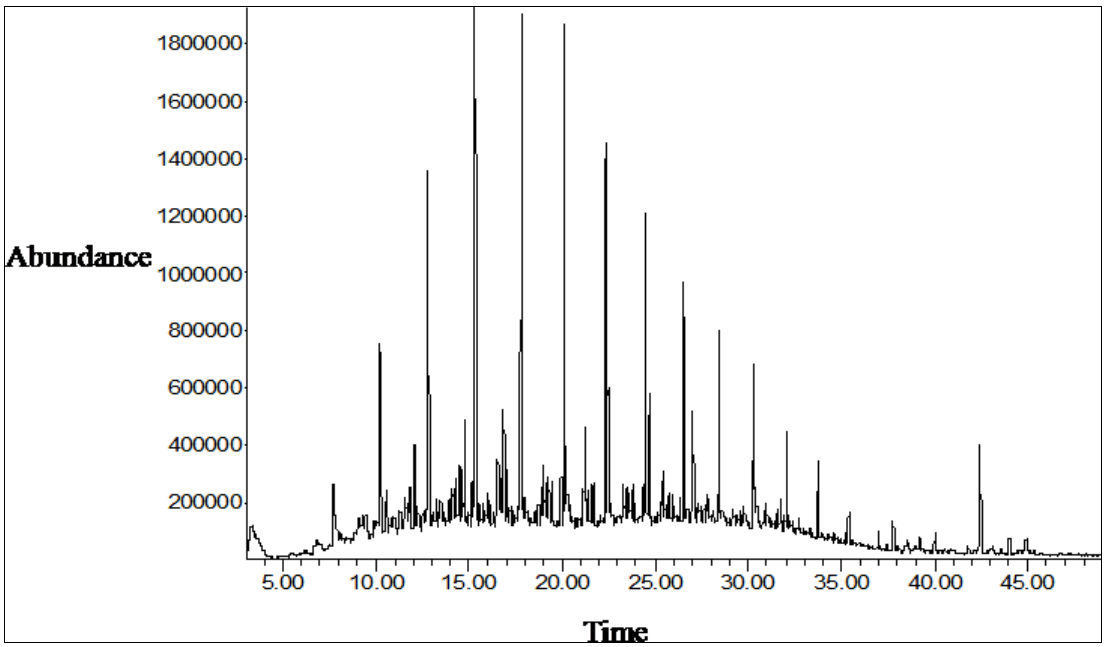

Fig 25: GC-MS chromatogram of *Acalypha indica* chloroform fraction (HIC).

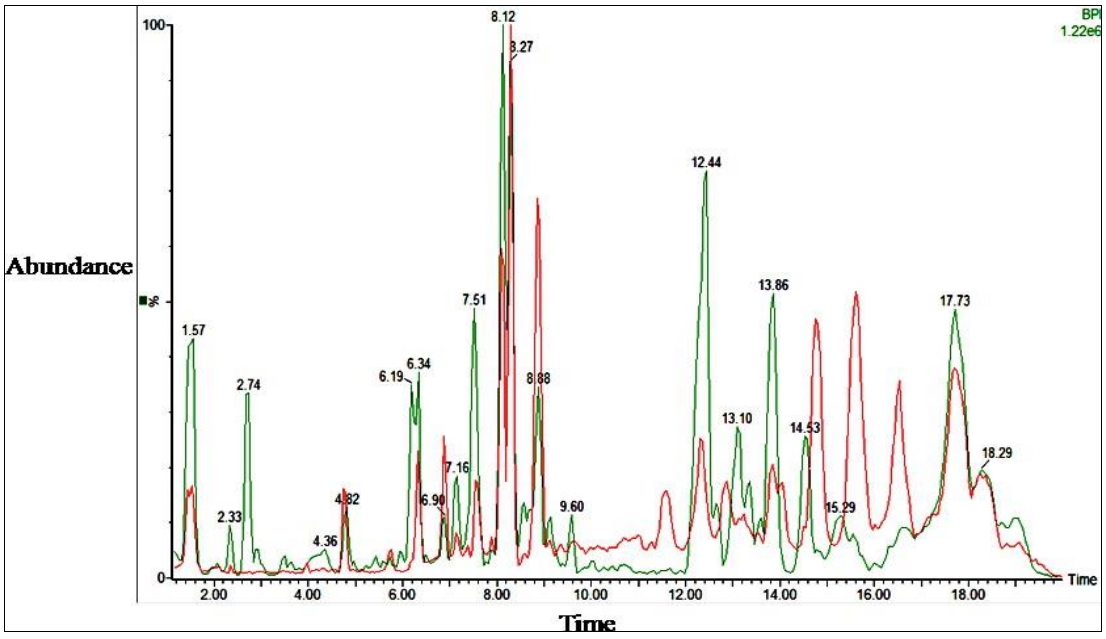

Fig 26: LC-MS chromatogram of *Acalypha indica* chloroform fraction (HIC). Green and red lines correspond to low and high energy chromatograms respectively.

Table 4: LC-MS/MS analysis of *Acalypha indica* chloroform fraction (HIC).

RT (Min)	Probable compound	Method
0.95	Indicine N-Oxide	Mono isotopic mass
1.46	Heliotrine	Mono isotopic mass
2.02	Rapanone	ReSpect database
2.32	Indicine	Mono isotopic mass
3.29	3-methoxy cinnamic acid	MZ cloud database
5.53	Rutin	MZ cloud database
6.59	Catechin	MZ cloud database
7.25	α-Eleostearic acid	MZ cloud database
8.73	Stearic acid	MZ cloud database
9.59	Diethyl phthalate	MZ cloud database

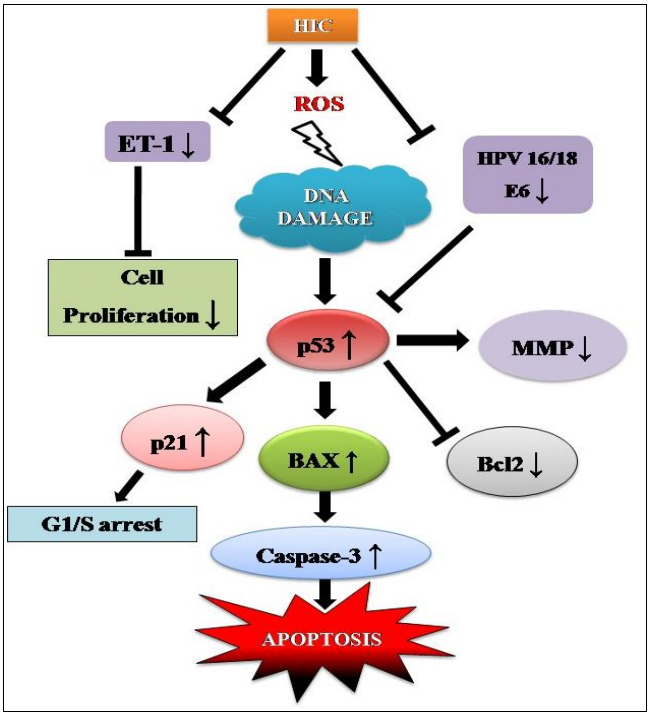

Fig 27: Hypothetical diagram showing the mode of action of the HIC fraction on the cervical cancer cells

Conclusion

The findings of this study indicate that the HIC fraction possesses significant potential to induce apoptosis in cervical cancer cells. The mechanism of action appears to involve ROS-mediated DNA damage, which contributes to cell death. Evidence of single-strand DNA damage was observed in the treated cells, along with activation of the ATR signalling pathway, supporting this mechanism. Furthermore, the HIC fraction was found to be rich in bioactive compounds such as cytotoxic fatty acids, phenolic compounds, and specific alkaloids. These results suggest that this fraction of *Acalypha indica* may serve as a promising source for the development of therapeutic agents against cancer.

References

1. Ahmadi M, Abdollahi R, Taherkhani A, *et al*. Herbal isolates in cervical cancer therapy. Genomics Inform,2024:22:9. https://doi.org/10.5808/gi.22079
2. AlMousa LA, Pandey P, Lakhanpal S, Kyada AK, H M, Nayak PP, *et al*. Anticancer potential of pentacyclic triterpenes: mechanisms and applications. Front Pharmacol,2025:16:1594901.
3. Astragalus polysaccharides combined with chemoradiotherapy for cervical cancer: A systematic review and meta-analysis. PMC / Clinical Oncology Studies, 2025.
4. Balachandran A, *et al*. Phytochemical screening and antioxidant potential. Molecules,2023:28:1043. https://doi.org/10.3390/molecules28031043
5. Bray F, *et al*. Global cancer statistics 2024. CA Cancer J Clin,2024.
6. Bykov VJ, *et al*. Targeting mutant p53 in cancer therapy. Nat Rev Cancer,2022. https://doi.org/10.1038/nrc.2022.XXX
7. Calotropis procera extract induces ROS-mediated apoptosis. J Ethnopharmacol,2025. https://doi.org/10.1016/j.jep.2025.117534
8. Chapkin RS, *et al*. Fatty acids and cancer prevention. J Nutr Biochem,2022.
9. Chekuri S, Vyshnava SS, Somisetti SL. Isolation and anticancer activity of quercetin from *Acalypha indica*. 3 Biotech,2023:13:289. https://doi.org/10.1007/s13205-023-03670-4
10. Chekuri S, Vyshnava SS, Somisetti SL. Isolation and anticancer activity of quercetin from *Acalypha indica* L. against breast cancer cell lines MCF-7 and MDA-MB-231. 3 Biotech,2023:13(8):289.
11. Dilkalal A, Annapurna AS, Umesh TG. Antioxidant and anticancer activity of polyphenol-rich plant extracts. Sci Rep,2024:14:28374.
12. Dilkalal A, Annapurna AS, Umesh TG. Polyphenols induce ROS-mediated apoptosis. Sci Rep,2024:14:28374. https://doi.org/10.1038/s41598-024-79996-7
13. Du C, *et al*. *Acalypha australis* induces ROS-mediated autophagic cell death via AKT/mTOR pathway suppression. Frontiers in Oncology,2026:16.
14. Hayati EK, Sabarudin A, Rafi M, Aulanni'am A, Firdaus A. In silico evaluation of anticancer activity of *Acalypha indica* bioactive compounds targeting ERα receptor. Proc Int Conf Green Technol,2025.
15. Hayati EK, *et al*. In silico anticancer evaluation of phytochemicals. Proc Green Technol, 2025.
16. Huang S, *et al*. Anti-cervical cancer mechanism of Ziyuglycoside I via molecular and experimental approaches. Scientific Reports,2025:15:36258.
17. Islam MA, *et al*. In silico study of phytocompounds targeting HPV-16 E6 protein for cervical cancer therapy. Scientific Reports,2024:14:17182.
18. Islam SI, *et al*. Investigating new drugs from marine metabolites for cervical cancer therapy using molecular dynamics. Scientific Reports,2025:15:3866.
19. Kalsoom A, Altaf A, Sarwar M, *et al*. GC–MS analysis and cytotoxic effect in HeLa cells. Sci Rep,2024. https://doi.org/10.1038/s41598-024-69582-2
20. Kiran A, *et al*. Cytotoxic potential of plant extracts. Sci Rep,2023:13:11376. https://doi.org/10.1038/s41598-023-11376-0
21. Lee JY, *et al*. Unsaturated fatty acids and cancer inhibition. Biochim Biophys Acta,2023.
22. Medicinal plants for overcoming drug resistance in cervical cancer. Front Pharmacol,2025. https://doi.org/10.3389/fphar.2025.XXXXX
23. Nair PMK, Pandian AR, Mathapati V, Tantry BS, Sai AS, Pai NP, *et al*. Anticancer potential of traditional medicinal plants from Tamil Nadu: a review. Front Immunol,2025:16:1680062.
24. Nair PMK, *et al*. Anticancer potential of traditional plants. Front Immunol,2025:16:1680062. https://doi.org/10.3389/fimmu.2025.1680062
25. Qian S, Wei Z, Yang W, *et al*. Role of Bcl-2 family proteins in apoptosis. Front Oncol,2022:12:985363. https://doi.org/10.3389/fonc.2022.985363
26. Rekha M, *et al*. Apoptosis and ROS analysis in plant extracts. J Maxillofac Oral Surg,2024.
27. Rekha M, *et al*. Comparative analysis of *Annona muricata* extract on cancer cells through apoptosis, ROS, MMP, and cell cycle analysis. Journal of Maxillofacial and Oral Surgery,2024.
28. Rutin isolated from *Acalypha indica* L.: A comprehensive analysis of its antibacterial and anticancer activities. Biochemical and Biophysical Research Communications,2025:765:151833.
29. Saravanan R, Raja K, Shanthi D. GC–MS and docking of phytocompounds. Appl Biochem Biotechnol,2022. https://doi.org/10.1007/s12010-021-03698-3
30. Sharma D, Sharma S, Mandal V, Dhobi M. Anti-inflammatory and pharmacological potential of *Acalypha indica*: a comprehensive review. Naunyn Schmiedebergs Arch Pharmacol,2024:397(4):1935-1956.

31. Sharma D, Singh C, Thakur AK, Apparsundaram S, Dhobi M. Therapeutic potential of standardized *Acalypha indica* extract in experimental models. Chem Biodivers,2025:22(11):e01226.
32. Sharma D, Singh C, Thakur AK, *et al*. Pharmacological potential of *Acalypha indica*. Chem Biodivers,2025:22:e01226. https://doi.org/10.1002/cbdv.202400226
33. Shimu MSS, Paul GK, Dutta AK, Kim C, Saleh MA, Islam MA, *et al*. Biochemical and molecular docking-based strategies of *Acalypha indica* and *Boerhavia diffusa* extract targeting cancer proteins. J Biomol Struct Dyn,2025:43(7):3330-3347.
34. Study on phytochemical composition and cytotoxic activity of plant extracts in cancer models. Antibiotics,2024:13(12):1193.
35. Study on plant-mediated nanoparticles using *Acalypha indica* and their anticancer activity. Onano,2024:100220.
36. Upadhyay S, *et al*. Exploring the ROS-mediated anticancer potential in human triple-negative breast cancer by garlic bulb extract. Journal of Traditional and Complementary Medicine,2024.
37. Upreti S, *et al*. ROS-mediated anticancer activity. J Tradit Complement Med,2024. https://doi.org/10.1016/j.jtcme.2024.
38. Venkatesan U, Muniyan R. Therapeutic potential of *Acalypha indica* leaf fractions: *in vitro* and in silico study. Sci Rep,2026:16:2423.
39. Venkatesan U, Muniyan R. Therapeutic potential of *Acalypha indica* leaf fractions. Sci Rep,2026:16:2423. https://doi.org/10.1038/s41598-025-32216-2
40. Westphal D, *et al*. Bax/Bak-mediated apoptosis mechanisms. PNAS,2022. https://doi.org/10.1073/pnas.1415142111